Biosensors and Bioelectronics 124–125 (2019) 244–252

Contents lists available at ScienceDirect

Biosensors and Bioelectronics

journal homepage: www.elsevier.com/locate/bios

# Multiple-layer guided surface acoustic wave (SAW)-based pH sensing in longitudinal FiSS-tumoroid cultures

Tao Wang[a,b,d,e], Ryan Green[a,c], Rasim Guldiken[a,b], Subhra Mohapatra[a,c], Shyam Mohapatra[a,d,e,f,*]

[a] Center for Research and Education in Nanobioengineering, University of South Florida, Tampa, FL 33612, USA
[b] Microfluidics and Acoustics Laboratory, Department of Mechanical Engineering, College of Engineering, University of South Florida, Tampa, FL 33612, USA
[c] Department of Molecular Medicine, Morsani College of Medicine, University of South Florida, Tampa, FL 33612, USA
[d] Department of Internal Medicine, Morsani College of Medicine, University of South Florida, Tampa, FL 33612, USA
[e] James A Haley VA Hospital, Tampa, FL 33612, USA
[f] College of Pharmacy Graduate Programs, University of South Florida, Tampa, FL 33612, USA

ARTICLE INFO

*Keywords:*
Surface acoustic wave (SAW)
Microfluidic
PH Sensor
Cancer
Tumoroids

ABSTRACT

A constitutively increased intracellular pH that is higher than the extracellular pH is emerging as a hallmark of cancer and determining pH could play a significant role in the measurement of drug responsiveness of tumor cells. However, a non-invasive, touch-free and real-time pH sensing as a research tool is lacking and remains a major unmet need. The purpose of the current study is to investigate a microfluidic surface acoustic wave (SAW) sensor platform capable of monitoring pH in cell and tumoroid cultures. A novel multi-layer guided SAW sensor integrated into a microfluidic channel was investigated theoretically and experimentally in detail for pH biosensing. Sensitivity and capability of the layer guided Love wave device was modeled using the finite element simulation. The model was verified experimentally, and a study monitoring pH of cell growth media is presented. This novel pH sensor is based on a 13.91 MHz center frequency SAW device coated with ZnO (500 nm) and $IrO_2$ (30 nm) layers to increase the sensitivity. A change in mechanical and electrical properties of the conductive $IrO_2$ layer was observed resulting from electrical corrosion induced by pH solutions affecting the charge distribution, SAW phase velocity and attenuation. By measuring the frequency shift induced by the change in SAW phase velocity between the test group and control group, the pH value of cell culture media from H460 cancer cell culture plates from day 0 to day 5 can easily be determined. To improve the sensitivity and stability of the sensor, a finite element method was used to optimize the layer thicknesses. Taken together, the results of experiments show the potential application of this device to be integrated with microfluidic channels and used in determining pH changes in longitudinal tumor cell cultures.

## 1. Introduction

Dysregulated pH is emerging as a hallmark of cancer because cancers show a 'reversed' pH gradient with a constitutively increased intracellular pH that is higher than the extracellular pH, which enables cancer progression by promoting proliferation (Kapus et al., 1993; Pouysségur et al., 1985; Srivastava et al., 2007; Stock and Schwab, 2009), the evasion of apoptosis (Lagadic-Gossmann et al., 2004; Matsuyama et al., 2000), metabolic adaptation (Christofk et al., 2008; Dietl et al., 2010; Kuwata et al., 1991), migration and invasion (Ayad et al., 2008; Martin et al., 2010). An increased understanding of pH sensors is expected to provide insight into the molecular basis for pH-dependent tumor cell behaviors, information on the central role of pH sensors in tumor cell adaptations and assistance in assessing tumor drug response. However, the approaches to determining pH changes in long-term tumor or tumoroid cultures are limited. Specifically, a non-invasive, touch-free and real-time pH sensing as a research tool remains a major challenge to advancing tumor cell biology (Vonau et al., 2005).

Thus, the measurement of pH values is a key parameter in cell biology as it serves as an indicator of important changes to the status and growth phase of cell cultures. The traditional pH glass potentiometric (Shibata et al., 2013; Vonau et al., 2005) has limitations, such as limited shape, large size and mechanical fragility, making it difficult to integrate into microfluidic culture platforms. MEMS-based pH sensors

* Correspondence to: Center for Research and Education in Nanobioengineering, University of South Florida, 12901 Bruce B. Downs Blvd., MDC019, Tampa, FL 33612, USA.
*E-mail addresses:* taowang@mail.usf.edu (T. Wang), rgreen1@health.usf.edu (R. Green), guldiken@usf.edu (R. Guldiken), smohapa2@health.usf.edu (S. Mohapatra), smohapat@health.usf.edu (S. Mohapatra).

https://doi.org/10.1016/j.bios.2018.10.011
Received 11 February 2018; Received in revised form 25 September 2018; Accepted 8 October 2018
Available online 12 October 2018
0956-5663/ 

have been widely studied, such as the ISFET pH sensor (Lu et al., 2018), capacitive pH sensor (Davidovikj et al., 2017), potentiometric pH sensor (Salazar et al., 2016) and conductimetric pH sensor (Y. Chen et al., 2013). The capacitive pH sensor is based on capacitive changes resulting from different concentrations of $H^+$ and $OH^-$ in the solution (Shamsul Arefin et al., 2014). The capacitive sensor is not an ideal choice for solutions containing multiple types of ions where each ion changes the capacitance of the solution. The ISFET pH sensor is a more complex sensor design which measures the current flow through a small conduction channel between source and drain (Hizawa et al., 2007). The ISFET pH sensor requires very high power for FET operations and a sophisticated fabrication process. A conductimetric pH sensor can measure the conductivity of a pH-responsive layer such as hydrogel or other polymers (Korostynska et al., 2007). The polymer sensing layer swells or shrinks in response to hydration caused by the pH of a solution. This sensor requires current flow through the sensing layer which is not applicable to most in vivo studies. The drawback of the conductivity pH sensor is that it is not ion-selective, and it measures the combined effect of all ions in the sample solution.

Many researchers have reported different new potentiometric pH sensors based on varies materials and structures. It was found that the metal oxide electrodes, such as $TiO_2$, $RuO_2$, $IrO_2$ and ZnO, have responses towards different pH solutions (Fog and Buck, 1984; Gill et al., 2008; Usman Ali et al., 2011; Xu and Zhang, 2010). However, most of them require a large amount of sample solution and voltage applied to the surface in contact with the cell culture media. Surface plasmon resonance (SPR) based fiber optic sensors have been used as a novel device to detect the pH of small amounts of liquid (Mishra and Gupta, 2013; Prabhash et al., 2017; Singh and Gupta, 2012). The pH measured by SPR is the result of the refractive index changes which are caused by the swelling/shrinkage of the hydrogel layer in response to different pH values. This sensor has a short response reaction time, good stability and good sensitivity. However, it has some disadvantages, such as high cost, large complex structure, high sensitivity to shock and bulky design.

There are different types of acoustic waves commonly used as biosensors. These include Rayleigh wave, Lamb wave, shear horizontal wave (SH-SAW) (including Love wave), Quartz crystal microbalance (QCM) and Thin-film bulk acoustic resonator (FBAR) (Bunroddith et al., 2018; Chen et al., 2015; Hsu et al., 2009; Onen et al., 2012a; Pantazis et al., 2010). For biomedical in vivo sensor design, elimination of the current and voltage flow in the media is a critical issue which requires low power consumption and touch-free design between electrode and media. The acoustic wave-based sensor has these natural advantages compared to ISFET, capacitive, potentiometric and conductimetric pH sensors. The FBAR operates at a very high frequency which can also create an ultra-high sensitivity (D. Chen et al., 2013; Wang et al., 2014). However, the FBAR can only detect the mass loading including the mass density and viscosity but cannot directly detect the conductivity and permittivity changes in the sample loading (Chen et al., 2017, 2015). QCM can add a pH reactive polymer layer to measure the polymer mass loading by shrinkage and swell (Ayad et al., 2010; Jagur-Grodzinski, 2006). Quartz crystal microbalances (QCM) are the most-commonly used BAW devices which are fabricated by sandwiching a bulk piezoelectric material with top and bottom metallic electrodes. QCM can excite a bulk thickness shear wave which can be used in both dry and liquid applications. However, the sensitivity and resolution of the QCM pH sensor are relatively low compared to SAW FBAR device (Fu et al., 2017). The propagated wave energy of Rayleigh wave and Lamb wave sensors is distributed not only across the substrate surface but also into the substrate. This causes the Rayleigh and Lamb waves to be directly coupled with the media on top and damped by the mass loading, which makes these two types of wave insensitive to the mass changes in liquid sensing (Onen et al., 2012b). The SH-SAW is composed of interdigital fingers (IDTs) fabricated as periodic rectangular electrodes with uniform lengths and gaps. Electrical stimulation of these IDTs creates the SAW used for biosensing. The guided wave in the SH-SAW (Love wave) can be enhanced by the layer properties to further concentrate the wave energy on the substrate surface and thus increase the sensitivity of the device. The Love wave device can create a very high sensitivity level similar to FBAR device but at a low frequency (Fu et al., 2017). Due to the low damping coupling in a liquid environment, SH-SAW and Love wave devices have already been widely used as gas and liquid sensors due to their high accuracy, label-free, touch-free sensing and small volume sample consumption capabilities (Wang et al., 2015). ST-cut Quartz and 36°Y-cut $LiTaO_3$ are the two the most common substrates to generate SH-SAW. However, the electroacoustic coupling coefficient ($K^2$) of ST-cut Quartz (0.0016) is much smaller than that of 36°Y-cut $LiTaO_3$ (4.7) (Lam et al., 2004; Pang et al., 2013).

Zinc oxide (ZnO) is a relatively common material in piezoelectric and photoacoustic fields. Many SAW devices are coated with ZnO to increase sensitivity and reduce insertion loss (Chang et al., 2006; Powell et al., 2004). These devices are used for different applications such as pH sensors, UV sensors and biosensors. Iridium oxide ($IrO_2$) is a widely used material for pH MEMS sensors which can provide a rapid and stable response in different media because of its high conductivity (Kakooei et al., 2013). The sensing principle is based on the transition function of electrical corrosion between two oxidation states (Baur and Spaine, 1998).

$$2IrO_2 + 2H^+ + 2e^- \leftrightarrow Ir_2O_3 + H_2O \quad (1)$$

In this study, we investigated the potential to enhance the sensitivity of oxide hydration changes to create a novel pH sensor with high sensitivity using a surface acoustic wave generation of a potential-distributed wave at the surface $IrO_2$ layer for longitudinal pH measurements in tumor cell cultures.

## 2. Experiment

### 2.1. Materials

A 99.5% purity 2" diameter and 0.125" thick $IrO_2$ target bonded with cooper backplate and a 99.9% purity 2" diameter and 0.125" thick ZnO target bonded with cooper at backplate were purchased from AJA international Inc (MA, USA). 36°Y-cut X propagated $LiTaO_3$ wafers were purchased from University Wafer Inc (CA, USA) and two gain RF amplifiers (Olympus 5073PR and Olympus 5072PR) were purchased from Olympus NDT Inc (Santa Clara, CA, USA). A digit frequency counter Agilent 53220A was purchased from Agilent Technologies Inc (Santa Clara, CA, USA) and an oscillator Tektronix TS2001C was purchased from Tektronix Inc (Beaverton, OR, USA). BenchVue Universal Counter software was licensed by Keysight Technologies (Santa Clara, CA, USA). H460 cell line was purchased from American Type Culture Collection (Manassas, VA, USA). HyClone™ RPMI 1640 culture media was purchased from GE Healthcare Life Scences (Pittsburgh, PA, USA). Commercial pH meter was purchased from Denver Instrument (Co, USA). Standard pH buffer solution was purchased from Sigma-Aldrich (WI, USA), Slygard@184 Silicone Elastomer kit was purchased from Dow Corning Inc (MI, USA). Hoechst 33342 was purchased from NucBlue, Life Technologies (MA, USA).

### 2.2. Design and fabrication of bio-sensor

Before the fabrication, a guide layer sensitivity comparison between ZnO and $IrO_2$ was investigated by using the wave perturbation theory. A thorough parametric study on sensitivity and perturbation was done for ZnO and $IrO_2$. The results were compared to optimize the design. The wave transmission study was based on a full time-dependent analysis to obtain the dynamic response of the impulse signal simulated devices in order to study the electrical perturbation on the substrate surface and find the limitation of the device. The final layer thickness

**Table 1**
Device parameters used for the simulation and fabrication of the IDT transducers.

| Parameters | Settings |
|---|---|
| Wavelength (λ) | 300 μm |
| Number of reflecting fingers | 30 pairs |
| Finger width | 75 μm |
| Wavelength of reflecting fingers | 297 μm |
| Number of fingers | 30 pairs |
| Well diameter | 6.5 mm |
| SAW velocity | 4160 m/s |
| ZnO layer thickness | 500 nm |
| IrO2 layer thickness | 30 nm |
| Operation frequency | 13.91 MHz |

was varied to balance the sensitivity and the wave transmission reflection ratio. Then the IDTs were fabricated by microfabrication techniques with feature parameters listed in Table 1. Further detail on the fabrication process can be found in our earlier publication (Guldiken et al., 2012). The ZnO film was deposited by an RF sputtering system at a deposition rate of about 120 nm per hour under a low substrate temperature of 180 °C, with 6sccm Ar and 6sccm $O_2$, and a 100 W RF power. The $IrO_2$ thin film was also deposited by RF sputtering. Prior to deposition, the chamber was pumped down to $1 \times 10^{-8}$ Torr. The substrates for sputtering substrates were 36 Y-cut X propagated lithium tantalate with transducer features on top (chrome layer 100 nm). Sputtering was performed in a pure Ar environment with a lower RF power of 80 W to mitigate potentially damaging bombardment of the growing $IrO_2$ film. We also used room temperature which generates lower stress on the surface of lithium tantalate piezoelectric material since the $IrO_2$ is a conductive metal oxide.

### 2.3. Preparation of cell culture media

For growing cell tumoroid cultures, we used a fiber-inspired smart scaffold (FiSS) developed by our lab, which generates tumor-like organoids from seeded tumor cells, hence called tumoroids. FiSS was prepared by electrospinning as described previously (Girard et al., 2013). FiSS was placed into a 6 well plate and 200,000 H460 lung cancer cells were seeded into each well in RPMI media containing 10% fetal bovine serum and 1% penicillin-streptomycin. Media (7 mL) was used in each well and cells were cultured on the scaffold for six days. Successful growth of cells on 3D scaffold as tumoroids was confirmed by staining the cells with Hoechst 33342 and then capturing images using fluorescence microscopy.

### 2.4. Experiment protocol for SAW measurement

H460 human lung adenocarcinoma cells were maintained in RPMI media containing 10% fetal bovine serum (FBS) and 1% penicillin-streptomycin. All cells were cultured in 6 well plates in a humidified incubator at 37 °C in a 5% $CO_2$ atmosphere. 1 mL of cell media supernatant in total was collected from a different well each day from day 0 to day 5. Half a minute after the frequency counter started to record, 100 μL of each culture media was placed on the test well of the chip and 100 μL of fresh culture media was taken from the same incubator and placed on the control well to record the relative frequency response for a duration of 10 min. A standard laboratory potentiometric pH meter was calibrated with standard pH buffer solution and then cleaned prior to each measurement of cell culture media at the same time to compare the pH value from the device. After recording each sample, the cell suspension was removed and the well was washed with three changes of PBS followed by three changes of water to clean the sensing area.

The frequency changes were measured by comparing the frequency shift between the test group to the control group as shown in Fig. 1. During the experiments, the frequency counter measures the frequency

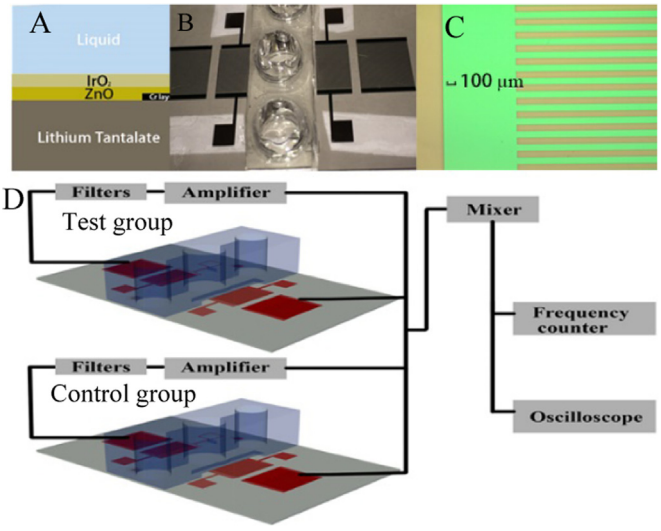


**Fig. 1.** (A) Conceptual view of the double guide layer of SAW sensor. (B) Fabricated and assembled resonator and fluidic well. (C) The finger pairs under the microscope. (D) Illustration of the experiment setup.

shift in two groups at the same time and transfers the real-time data to the computer. With the help of the BenchVue software, a programmed data flow process handles the 6 data points generated by each group every second. The software records and plots the control group recorded frequency ($f_c$) minus the test group recorded frequency ($f_T$) then divides by the control group recorded frequency ($f_c$). From the perturbation theory, when the Love waves propagate through the sensing area, the phase velocity changes due to the mass loading changes at the surface of the $IrO_2$ and the conductivity of the cell media in Eqs. (2) and (3). The data is then sorted by Matlab© and plotted out in normalized relative frequency shift.

Change in velocity:

$$\frac{\Delta V}{V} = \frac{\Delta f}{f} = \frac{f_C - f_T}{f_C} = \frac{K_S^2}{2}\frac{(\sigma_1/\omega)^2+(\varepsilon_1 - \varepsilon_{REF})(\varepsilon_1 + \varepsilon_{PIEZO})}{(\sigma_1/\omega)^2 + (\varepsilon_1 + \varepsilon_{PIEZO})^2} \quad (2)$$

Change in attenuation:

$$\frac{\Delta \alpha}{k} = \frac{K_S^2}{2}\frac{(\sigma_1/\omega)(\varepsilon_{REF} + \varepsilon_{PIEZO})}{(\sigma_1/\omega)^2 + (\varepsilon_1 + \varepsilon_{PIEZO})^2} \quad (3)$$

## 3. Results and discussion

### 3.1. Multiple layer perturbation analysis

A numerical method was designed to optimize the thickness of the $IrO_2$ and ZnO thin film layer as a guiding layer. The mathematical model was based on previous reports from the perturbation analysis model (McMullan et al., 2000; Onen and Guldiken, 2014). The substrate and the guiding layers were assumed to be elastic and isotropic materials without significant electrical perturbation. The analysis is based on the dispersion equation and sensitivity equation (Eqs. (1) and (2) in the Supplementary material) verified by McHale et al. (2002) which depends on the dispersion curve, guiding and perturbing mass layer properties (Onen, 2013). Other leaky properties of SH or SSBW waves were also neglected, since only the Love waves were effective in energy confinement to the surface. The analysis was performed with the non-dimensional thickness (z) defined as $z = d_g \bullet f / v_g^{\infty}$, where $d_g$ is the thickness, $f$ is the frequency and $v_g^{\infty}$ is the shear velocity in guiding layer. Shear horizontal polarized wave propagation was investigated step by step by dispersion solution and perturbation analysis (McMullan et al., 2000; Onen and Guldiken, 2014).

The comparison of the ZnO and $SiO_2$ layer sensitivity on the device

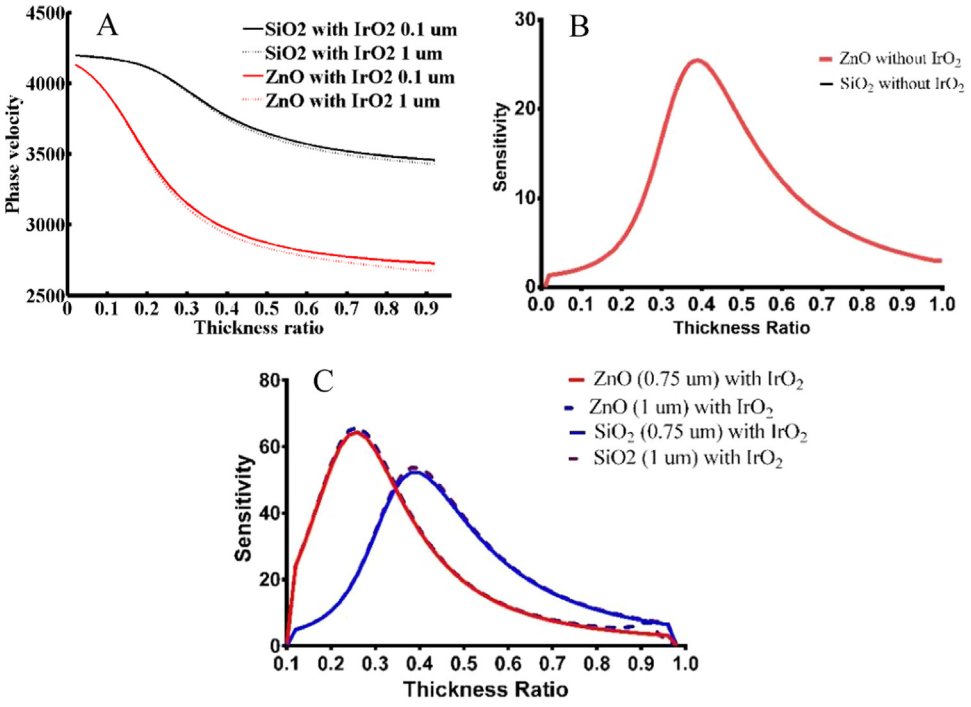


**Fig. 2.** (A) Dispersion curve with $SiO_2/IrO_2$ and $ZnO/IrO_2$ guiding layer at 14.0 MHz (B) Perturbation analysis method to calculate the sensitivity of multiple layers SAW-based sensor. At the single layer mode, the sensitivity of the $SiO_2/LiTaO_3$ is almost the same as $ZnO/LiTaO_3$ device. (C) The $IrO_2/ZnO/LiTaO_3$ create higher sensitivity with thin layer thickness requirement compared to $IrO2/SiO_2/LiTaO_3$.

is shown in Fig. 2. Fig. 2A illustrates the dispersion curve of two different guiding layers with the same top layer of $IrO_2$. The $SiO_2$ dispersion curves have smoother transition regions and lower slopes. The lower slopes illustrate a smaller velocity difference between the substrate and guiding layer which results in lower sensitivity (Onen and Guldiken, 2014). Fig. 2B shows the device model with a fluid layer and a single pure guide layer on top of the substrate (Liquid/ZnO/$LiTaO_3$ and Liquid /$SiO_2$/$LiTaO_3$). This figure shows that the $SiO_2$ and $IrO_2$ have similar sensitivity at the same thickness ratio (film thickness divided by wavelength) with the peak sensitivity at thickness ratio (guide layer thickness/wavelength) $\varepsilon = 0.42$. But after the $IrO_2$ layer is deposited on top of the ZnO layer, the ZnO layer revealed two advantages compared to $SiO_2$. Fig. 2C shows that ZnO has higher sensitivity than the $SiO_2$ layer and it also reduced the layer thickness requirement to reach maximum sensitivity by almost half ($\varepsilon_{ZnO} = 0.24$, $\varepsilon_{SiO2} = 0.42$). ZnO significantly reduced the layer thickness requirement to create high sensitivity for the device. From these results, the maximum sensitivity is created at the thickness ratio of ZnO equal to 0.24 with almost 2-fold sensitivity compared to the pure ZnO guiding layer's maximum sensitivity peak. However, the perturbation analysis is based on the theory of a linear elastic model with lossless substrate and it is hard to show the electric perturbation on the surface.

Acoustic propagation mass sensing within multi-thin-layer systems is essential for optimization of gravimetric sensors. Perturbation analysis is an easy method to set up a simplified model. The actual wave propagation problem on the piezoelectric substrate involves an anisotropy layer, piezoelectricity, and three-dimensional wave diffraction. It is very complicated and not feasible for numerical methods to model all of these features. It is also not possible for numerical methods to analyze the electrical properties of the wave mode such as velocity phase, electrical perturbation, and wave transmission. The finite element method provides a more suitable method to analyze the wave transmission and electrical perturbation. The deposited ZnO is a piezoelectric guiding layer for this Love device, and the $IrO_2$ thin layer on top of ZnO works as both a guiding layer and pH sensitive layer. Due to the conductive properties of the metal oxide $IrO_2$, the conductivity of the $IrO_2$ and the media on top of the layer will affect the electrical perturbation on the guiding layer. Additionally, the electric equilibrium reaction at the surface will affect both the conductivity and the mass loading.

### 3.2. Finite element analysis

A COMSOL finite element model was built to simulate the wave propagation properties including the wave transmission, mass loading limitation and electrical perturbation on the substrate in Fig. 3. The simplified 3D model consists of a two-port resonator design with a ZnO thin layer and $IrO_2$ thin layer on top of a Lithium tantalate substrate with 4 mesh nodes per wavelength. The mesh consisted of 47,352 domain elements, 24,734 boundary elements and 2412 edge elements. The total number of nodes is 926,222 as shown in Fig. 3A. A time-dependent analysis was conducted to calculate the response from the interdigital output finger with a short impulse signal. The total sampling time for the whole simulation was 4400 ns (nano second) with a sampling frequency of 1000 MHz. The impulse voltage was applied to the input electrodes while $V_+$ and $V_-$ were applied to the even and odd fingers.

$$V_+ = \begin{cases} +1 \quad V, & 0 \ll t \ll 1 \quad ns \\ 0 \quad V, & t > 1 \quad ns \end{cases}$$

$$V_- = 0$$

Fig. 3B, C, and D show the electrical potential distribution at the surface of the device and the mechanical surface wave's electrical propagation along the detection area from 0 ns to 1500 ns. The simulation results in Fig. 3E and F were verified by the fabricated device. In Fig. 3E the simplified 3D model with 100 nm Cr IDTs, 500 nm ZnO and 30 nm $IrO_2$ layer matches the physical device's first two wave modes with peaks of 13.907 MHz and 15.34 MHz. However, due to the simplified 3D simulation model with only one single pair of input/output interdigital fingers and one reflecting finger for each side, the third and fourth mode of the wave is not perfectly matched with the experimental results. The mechanical wave phase velocity is affected by the mass loading and electrical properties of the surface and media. The simulation results show that the surface acoustic wave energy loss increases at the surface when the thickness of the $IrO_2$ thin layer increases as compared in Fig. 3E and Fig. 3F. The surface acoustic wave is damped by the $IrO_2$ thin layer and starts to cease propagation at a thickness of

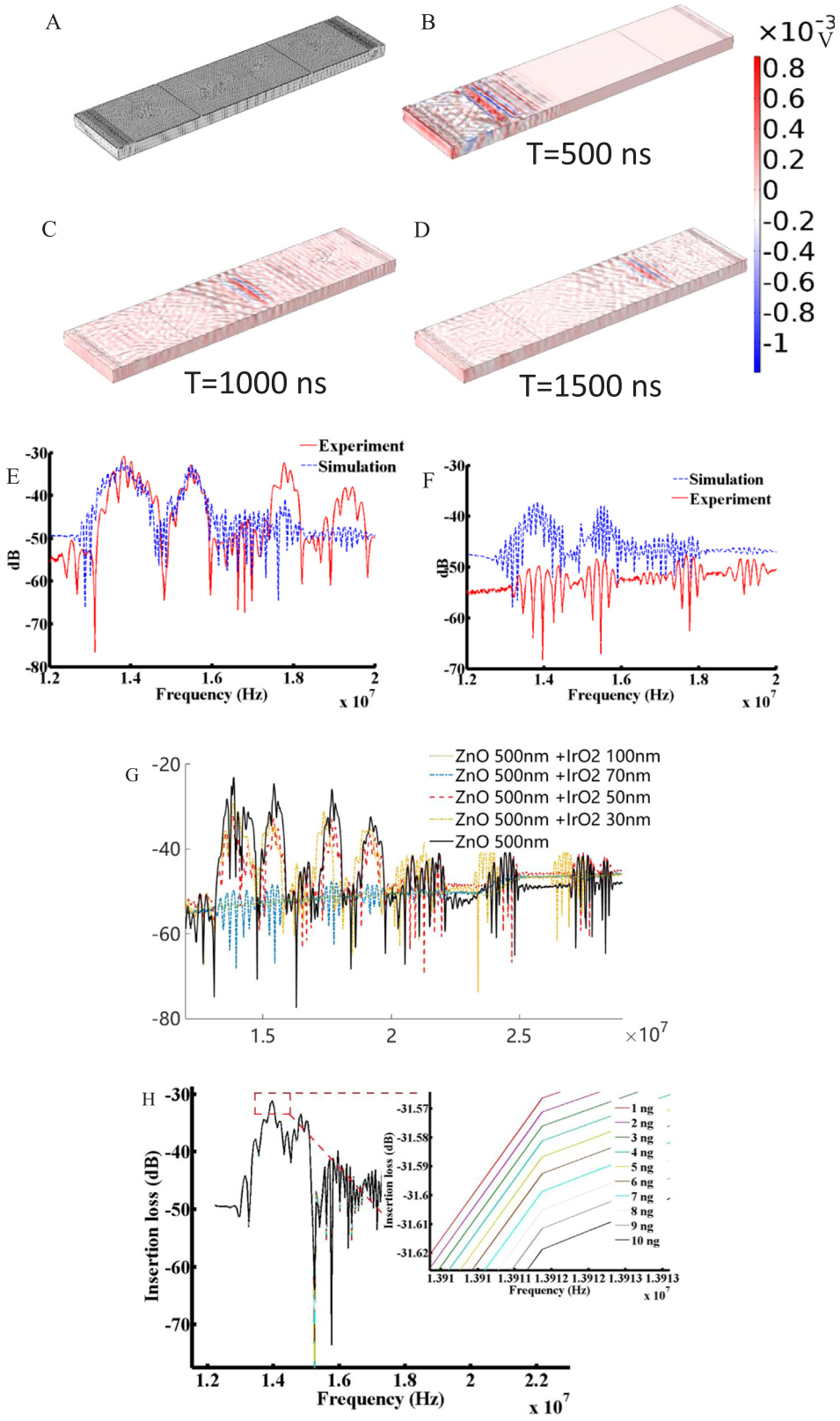


**Fig. 3.** (A) Completed mesh of the model with one pair of IDTs (interdigital transducers) and one pair of reflecting fingers at both input and output port. (B), (C) and (D) are the surface acoustic wave electrical perturbation at the surface of Lithium Tantalate. (E) Comparison between simulation and experiment frequency response for the device (with 100 nm Cr IDTs + 500 nm ZnO + 30 nm $IrO_2$) from 12 MHz to 20 MHz. (F) Comparison between simulation and experiment frequency response for the device (with 100 nm Cr IDTs + 500 nm ZnO + 70 nm IrO2) from 12 MHz to 20 MHz. (G) The frequency spectrum of different $IrO_2$ coating layers on the device measured by the network analysis. Increasing the $IrO_2$ layer on the top of the device decreases the Insertion loss. After depositing ~100 nm $IrO_2$ on the surface, the acoustic wave ceased propagating at the surface by the conductive $IrO_2$ layer. (H) The device model response to different mass loading changes of the $IrO_2$ layer.

70 nm as shown in Fig. 3E. Fig. 3F shows that at the increased thickness of $IrO_2$ device of 70 nm compared to the thickness 30 nm in Fig. 3E, the transmission ratio reduces from −32.6 dB a lot to −37 dB. The experimental device reduces the transmission ratio from −30.8 dB to −50.3 dB. The simulation results match the experiment results in Fig. 3F. However the transmission ratio is 13.3 higher than the experiment. The operation frequency of the device slightly decreases as the thickness of the $IrO_2$ increases both in the simulation results and experiment results in Fig. 3F and in Fig. 3G. The mass loading changes at the surface of the $IrO_2$ layer result in the phase velocity and frequency shift. In Fig. 3H, the simulation results illustrate that if the $IrO_2$ mass loading even slightly increases from 1 ng to 2 ng, the frequency

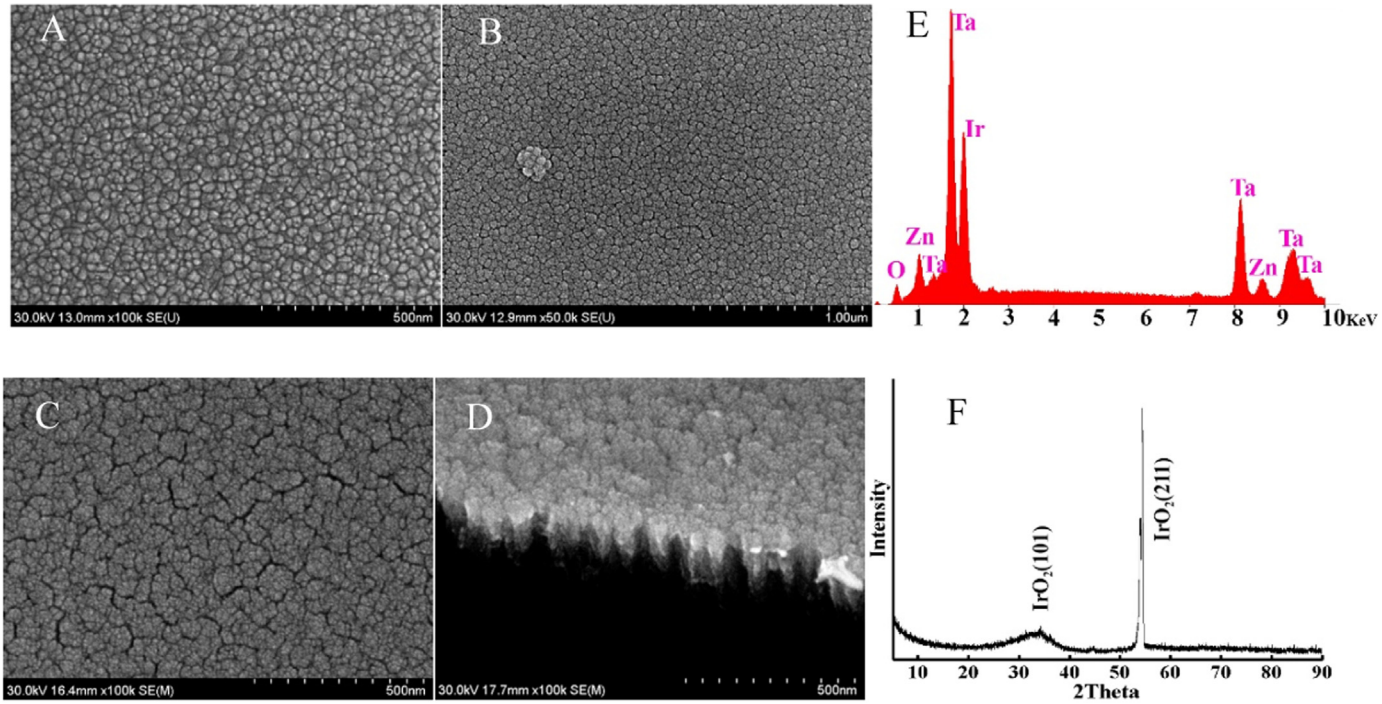


**Fig. 4.** (A) SEM surface topographical image of a ZnO thin film. (B) (C) and (D) SEM surface topographical image of a $IrO_2$ thin film. (E) EDS diffraction analysis of the device. (F) XRD diffraction analysis of the device to find the 2theta for the $IrO_2$ thin layer.

decreases and the insertion loss goes down.

### 3.3. Morphology of the guiding layer

After the device was fabricated, the SEM, XRD, and EDS images were captured to investigate the morphology of the ZnO and $IrO_2$ layers as illustrated in Fig. 4. Fig. 4A is an SEM surface topographical image at 100 K magnification of a ZnO thin film with thermal annealing at 300 °C. The image shows that the surface of the RF deposited ZnO thin flat film layer. Fig. 4B and Fig. 4C is the topographical image at 50 K and 100 K magnification of the $IrO_2$ thin film layer. Fig. 4D is the cross-section view of the $IrO_2$ layer. Fig. 4E and Fig. 4F is the EDS and XRD diffraction analysis of the device with ZnO and $IrO_2$ thin film layer. The $IrO_2$ has two peaks with 2theta at 34.7° and 54.3°.

### 3.4. Cell media measurements

Electrical perturbation occurs due to interactions between the electrical potential and the liquid. It is also referred to as acoustoelectrical interaction. The properties of the liquid that contribute to electrical perturbation are the conductivity (σ) and the permittivity (ε). The conductivity of the sampling solution is also related to frequency shift from Eqs. (2) and (3). The SAW propagated with multiple fluxes of momentum energy on the surface of $IrO_2$. The momentum will reduce to become a force on the electron which is also referred to as acoustoelectrical interaction. For the acid region, the conductivity of the film decreases the result of the interaction as the pH value increase. From Eq. (3), a larger σ leads a smaller phase velocity. Thus, the conductivity of the media layer increases as the phase velocity decreases. The resonant frequency of the propagated SAW is relative to the phase velocity at a fixed wavelengths device. Therefore, a decrease of the resonant frequency of the device should be detected on low pH media. In Eq. (1) when the pH value decreases, it will result in more $IrO_2$ translating to $Ir_2O_3$, which will slightly decrease the mass of the $IrO_2$ layer and slightly increase the frequency as shown in the simulation results Fig. 3H. There is only maximum ~1.7 ng mass changes if all the $IrO_2$ translates to the $Ir_2O_3$ in the detection well. In the simulation results Fig. 3H, 2 ng mass changes lead to less than 400 Hz shift. The shifts of charge distribution on ZnO layer caused by changes in $IrO_2$ layer's electrical properties dominate the phase velocity changes. Similar analysis shows the expected results in the alkaline region, as the interaction between hydroxide and metal oxide layer ($IrO_2$ and ZnO) also enhances the guiding layer conductivity (Qiu et al., 2011).

A standard pH buffer solution was prepared to calibrate the response of the device to different pH solutions both inside the incubator and at atmosphere outside the incubator. The $CO_2$ level and temperature inside the incubator affect the pH and function of the device. The device calibration determines the relationship of the relative frequency shift to standard pH value both in the incubator and at atmosphere. The change in $IrO_2$ relative permittivity and electrical conductivity due to the metal oxide corrosion on the surface will result in the phase velocity of the propagated wave shift. As discussed previously, the relative frequency shift is equal to the frequency of the reference device minus the working device divided by the reference frequency. The operation frequency of the working device decreases as the pH value decreases as both the relative permittivity and the electric conductivity increase. The relationship between the pH value and frequency shift is nonlinear due to the nonlinear change of the conductivity and mass loading which shows the polynomial fit curve in Fig. 5. Both the fit curves for atmosphere and incubator environment have the $R^2 = 0.99$. At pH 3, the device has a maximum frequency shift of 0.296 ppm (0.000296). The frequency shift at atmosphere is larger than the shift inside the incubator which is to be expected. The relationship between the standard pH value and the relative frequency shift provides the conversion equation to convert the relative frequency to pH value for cell culture experiments.

After the pH value of the standard solution is recorded, a pH value of cell culture media is measured from day 0 to day 5. The frequency shift from day 0 to day 1, day 4 to day 5 is much smaller than the frequency shift from day 2 to day 3, from day 3 to day 4. A maximum 0.0591 ppm (0.0000591) was measured at day 5 as illustrated in Fig. 6A. Additionally, the relative frequency shift on the y-axis in Fig. 6A is converted to standard pH value by the relationship in Fig. 5 and replotted in Fig. 6C (atmosphere) and Fig. 6D (incubator). The cell

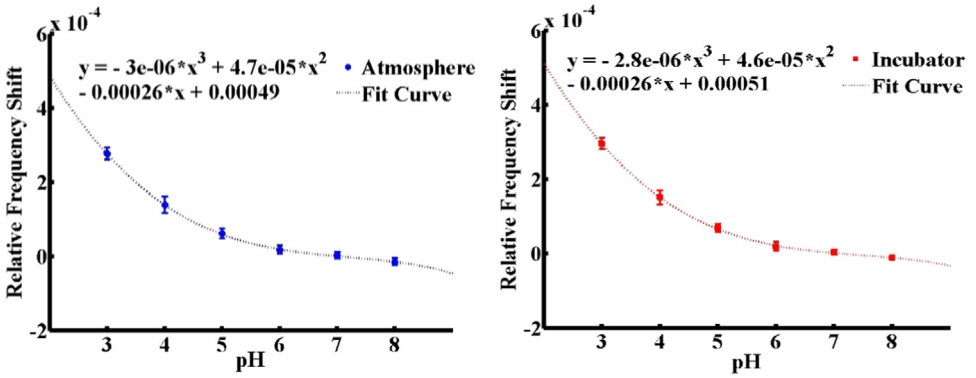


**Fig. 5.** (A) The SAW-based sensor is tested by standard pH solutions to record the frequency response. Since the $CO_2$ concentration and temperature will affect the pH, pH is measured both inside incubator and at atmosphere.

media from day 0 to day 5 was also measured by commercial instrument and compared to the $IrO_2$/ZnO/$LiTaO_3$ device in Fig. 6 C and D. We found that the SAW acoustic device measured pH value was 1.0–3.05% smaller than the value from the commercial device value at atmosphere, and 2.25–3.75% smaller than the value from the commercial device value inside the incubator. This discrepancy could be caused by several factors. First, the conversion from the average frequency shift to standard pH includes a calculation error. Second, the cell culture media from day 1 to day 5 is slightly different than unused cell media on the working device in its mechanical and electrical properties such as density and dielectric constant. Third, the ZnO layer may contribute an effect to the phase velocity of the device. The ZnO/$LiTaO_3$ SAW-based (500 nm ZnO layer) device without $IrO_2$ layer is tested by standard pH solutions at atmosphere to record the frequency response. Fig. S6 shows that without the $IrO_2$ layer, the ZnO sensitivity is quite low compared to the device with $IrO_2$ layer Fig. 5.

The experiment results show the advantage of the unique design by using multiple layers. The ZnO layer works as a guiding layer helping the wave propagation to concentrate energy and charge potential at ZnO layer which increases the sensitivity of the device. ZnO also works as a dielectic shield layer between the IDT fingers and $IrO_2$ conductive layer. The most important feature is that waves propagating at the ZnO intermediate layer can be easily affected by changes in electrical properties through the conductive IrO2 layer. Therefore, piezoelectric surface charge and the voltage potential at the ZnO layer will be affected by the $IrO_2$ layer's chemical reaction and charges. We compare our design to other acoustic-based pH sensors in Table 2. The device based on the bare ZnO layer has a little high sensitivity by etching the surface ZnO, which has stability and repeatability issues and can only be used for the disposable device.

## 4. Summary and conclusions

In this study, a multi-layer guided surface acoustic wave sensor was investigated theoretically and experimentally in detail for pH bio-sensing. Shear horizontal layer guided surface acoustic wave (SAW) device

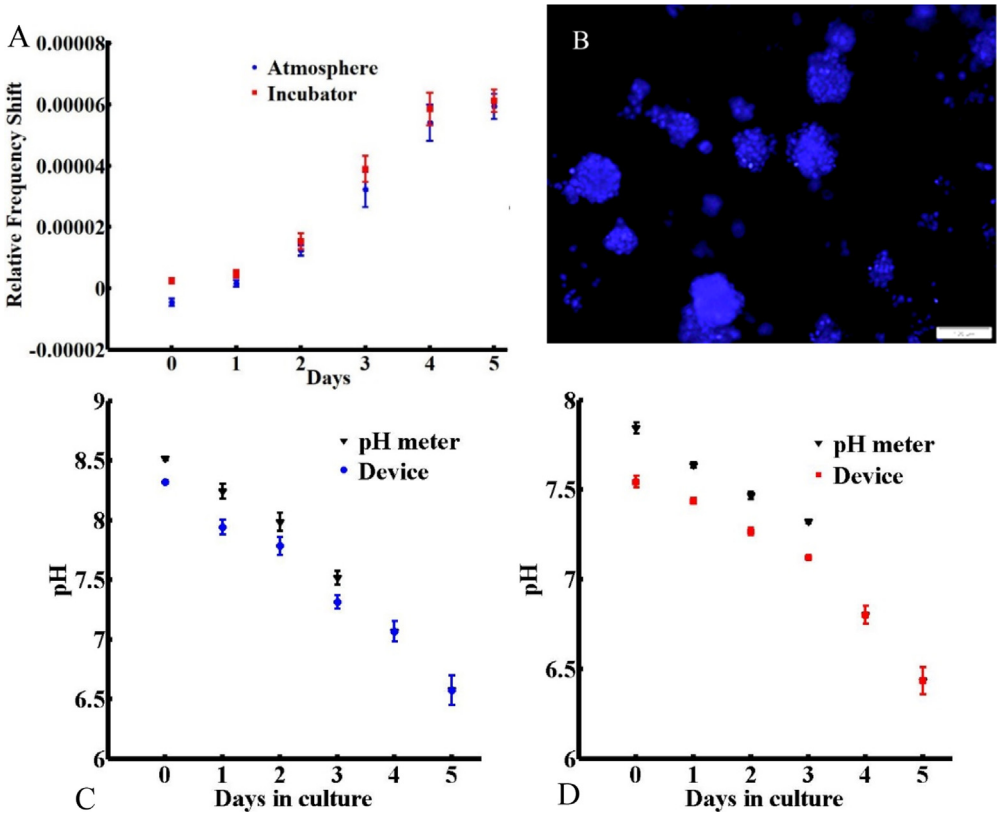


**Fig. 6.** (A) The relative frequency response of the device to cell culture media in different days both in atmosphere and incubator measurements. (B) Day 5 H460 tumoroids on scaffold stained with Hoechst. (C) The comparison between the commercial pH meter measured cell media pH value and device measured value at atmosphere from day 0 to day 5. (D) The comparison between the commercial pH meter measured cell media pH value and device measured value inside the incubator from day 0 to day 5.

**Table 2**
Comparison to other acoustic-based pH sensors.

| Literature | Type | Top layer material | Sensitivity ($(\Delta f/f)/pH$) | pH resolution |
|---|---|---|---|---|
| Qiu et al. (2011) | Single layer love wave | ZnO | $4.3 \times 10^{-4}$ | |
| Ayad et al. (2008) | QCM | Acid copolymer layer | $2.0 \times 10^{-5}$ | |
| This paper | Multiple layer love wave | $IrO_2$/ZnO | $5.9 \times 10^{-5}$ | 0.011 |

sensitivity and capability was modeled using perturbation analysis mode and finite element method. The model was verified experimentally, and a surface acoustic wave pH biosensor study was presented. A novel pH sensor based on 13.91 MHz center frequency SAW device was coated with ZnO and $IrO_2$ guided and sensitization layers to increase sensitivity. The change in conductivity of ZnO and $IrO_2$ induced by pH solutions affects SAW phase velocity and attenuation. By measuring the frequency shift induced by a change in SAW phase velocity between the work group and control group, the pH value in a target cell culture media can be determined. To improve the sensitivity and stability of the sensor, multiple methods to fabricate the ZnO layer on shear horizontal wave devices were compared. The results of experiments show the potential application of this device to be integrated with microfluidic channels used in cancer biology and in regenerative medicine.

## Acknowledgments

This research was supported by VA Merit Review Awards #BX003685 and BX003413, and Research Career Scientist Awards to Dr. Shyam Mohapatra (IK6 BX003778) and Dr. Subhra Mohapatra (IK6BX004212). Though this report is based upon work supported in part by the Department of Veterans Affairs, Veterans Health Administration, Office of Research and Development, the contents of this report do not represent the views of the Department of Veterans Affairs or the United States Government. The funders had no role in study design, data collection, and analysis, decision to publish, or preparation of the manuscript.

## Appendix A. Supporting information

Supplementary data associated with this article can be found in the online version at doi:10.1016/j.bios.2018.10.011.

## References

Ayad, M.M., Salahuddin, N.A., Abou-Seif, A.K., Alghaysh, M.O., 2008. PH sensor based on polyaniline and aniline-anthranilic acid copolymer films using quartz crystal microbalance and electronic absorption spectroscopy. Polym. Adv. Technol. 19, 1142–1148. https://doi.org/10.1002/pat.1106.

Ayad, M.M., Salahuddin, N.A., Alghaysh, M.O., Issa, R.M., 2010. Phosphoric acid and pH sensors based on polyaniline films. Curr. Appl. Phys. 10, 235–240. https://doi.org/10.1016/j.cap.2009.05.030.

Baur, J.E., Spaine, T.W., 1998. Electrochemical deposition of iridium(IV) oxide from alkaline solutions of iridium(III) oxide. J. Electroanal. Chem. 443, 208–216. https://doi.org/10.1016/S0022-0728(97)00532-9.

Bunroddith, K., Viseshakul, N., Chansiri, K., Lieberzeit, P., 2018. QCM-based rapid detection of PCR amplification products of Ehrlichia canis. Anal. Chim. Acta 1001, 106–111. https://doi.org/10.1016/j.aca.2017.10.037.

Chang, R.C., Chu, S.Y., Hong, C.S., Chuang, Y.T., 2006. A study of love wave devices in ZnO/quartz and ZnO/LiTaO3structures. Thin Solid Films 498, 146–151. https://doi.org/10.1016/j.tsf.2005.07.065.

Chen, D., Wang, J., Wang, P., Guo, Q., Zhang, Z., Ma, J., 2017. Real-time monitoring of human blood clotting using a lateral excited film bulk acoustic resonator. J. Micromech. Microeng. 27, 045013. https://doi.org/10.1088/1361-6439/aa5bbe.

Chen, D., Wang, J., Xu, Y., Li, D., Zhang, L., Li, Z., 2013. Highly sensitive detection of organophosphorus pesticides by acetylcholinesterase-coated thin film bulk acoustic resonator mass-loading sensor. Biosens. Bioelectron. 41, 163–167. https://doi.org/10.1016/j.bios.2012.08.018.

Chen, G., Zhao, X., Wang, X., Jin, H., Li, S., Dong, S., Flewitt, A.J., Milne, W.I., Luo, J.K., 2015. Film bulk acoustic resonators integrated on arbitrary substrates using a polymer support layer. Sci. Rep. 5, 1–8. https://doi.org/10.1038/srep09510.

Chen, Y., Mun, S.C., Kim, J., 2013. A wide range conductometric pH sensor made with titanium dioxide/multiwall carbon nanotube/cellulose hybrid nanocomposite. IEEE Sens. J. 13, 4157–4162. https://doi.org/10.1109/JSEN.2013.2261812.

Christofk, H.R., Vander Heiden, M.G., Wu, N., Asara, J.M., Cantley, L.C., 2008. Pyruvate kinase M2 is a phosphotyrosine-binding protein. Nature 452, 181–186. https://doi.org/10.1038/nature06667.

Davidovikj, D., Scheepers, P.H., van der Zant, H.S.J., Steeneken, P.G., 2017. Static capacitive pressure sensing using a single graphene drum. ACS Appl. Mater. Interfaces 9, 43205–43210. https://doi.org/10.1021/acsami.7b17487.

Dietl, K., Renner, K., Dettmer, K., Timischl, B., Eberhart, K., Dorn, C., Hellerbrand, C., Kastenberger, M., Kunz-Schughart, L.A., Oefner, P.J., Andreesen, R., Gottfried, E., Kreutz, M.P., 2010. Lactic acid and acidification inhibit TNF secretion and glycolysis of human monocytes. J. Immunol. 184, 1200–1209. https://doi.org/10.4049/jimmunol.0902584.

Fog, A., Buck, R.P., 1984. Electronic semiconducting oxides as pH sensors. Sens. Actuators 5, 137–146. https://doi.org/10.1016/0250-6874(84)80004-9.

Fu, Y.Q., Luo, J.K., Nguyen, N.T., Walton, A.J., Flewitt, A.J., Zu, X.T., Li, Y., McHale, G., Matthews, A., Iborra, E., Du, H., Milne, W.I., 2017. Advances in piezoelectric thin films for acoustic biosensors, acoustofluidics and lab-on-chip applications. Prog. Mater. Sci. 89, 31–91. https://doi.org/10.1016/j.pmatsci.2017.04.006.

Gill, E., Arshak, K., Arshak, A., Korostynska, O., 2008. Mixed metal oxide films as pH sensing materials. Microsyst. Technol. 14, 499–507. https://doi.org/10.1007/s00542-007-0435-9.

Girard, Y.K., Wang, C., Ravi, S., Howell, M.C., Mallela, J., Alibrahim, M., Green, R., Hellermann, G., Mohapatra, S.S., Mohapatra, S., 2013. A 3D fibrous scaffold inducing tumoroids: a platform for anticancer drug development. PLoS One 8. https://doi.org/10.1371/journal.pone.0075345.

Guldiken, R., Jo, M.C., Gallant, N.D., Demirci, U., Zhe, J., 2012. Sheathless size-based acoustic particle separation. Sensors 12, 905–922. https://doi.org/10.3390/s120100905.

Hizawa, T., Matsuo, J., Ishida, T., Takao, H., Abe, H., Sawada, K., Ishida, M., 2007. 32 X 32 pH image sensors for real time observation of biochemical phenomena. In: Proceedings of the 4th International Conference on Solid-State Sensors, Actuators and Microsystems TRANSDUCERS and EUROSENSORS '07, IEEE, pp. 1311–1312. https://doi.org/10.1109/SENSOR.2007.4300379.

Hsu, C.L., Shen, C.Y., Tsai, R.T., Su, M.Y., 2009. Surface acoustic wave ammonia sensors based on ST-cut quartz under periodic al structure. Sensors 9, 980–994. https://doi.org/10.3390/s90200980.

Jagur-Grodzinski, J., 2006. Nanostructured polyolefins/clay composites: role of the molecular interaction at the interface. Polym. Adv. Technol. 17, 395–418. https://doi.org/10.1002/pat.

Kakooei, S., Ismail, C., Ari-Wahjoedi, B., 2013. An overview of pH sensors based on Iridium oxide: fabrication and application. Int. J. Mater. Sci. Innov. 1, 62–72.

Kapus, A., Romanek, R., Qu, A.Y., Rotstein, O.D., Grinstein, S., 1993. A pH-sensitive and voltage-dependent proton conductance in the plasma membrane of macrophages. J. Gen. Physiol. 102, 729–760. https://doi.org/10.1085/jgp.102.4.729.

Korostynska, Olga, Arshak, Khalil, Gill, Edric, Arshak, Arousian, 2007. Review on key laboratory State-of-the-art in nonlinear mechanics polymer based pH mechanics, Sensors sciences. Sensors 7 (12), 3027–3042. https://doi.org/10.3390/s7123027.

Kuwata, F., Suzuki, N., Otsuka, K., Taguchi, M., Sasai, Y., Wakino, H., Ito, M., Ebihara, S., Suzuki, K., 1991. Enzymatic regulation of glycolysis and gluconeogenesis in rabbit periodontal ligament under various physiological pH conditions. J. Nihon Univ. Sch. Dent. 33, 81–90. https://doi.org/10.2334/josnusd1959.33.81.

Lagadic-Gossmann, D., Huc, L., Lecureur, V., 2004. Alterations of intracellular pH homeostasis in apoptosis: origins and roles. Cell Death Differ. 11, 953–961. https://doi.org/10.1038/sj.cdd.4401466.

Lam, C.S., 2010. A review of the recent development of temperature stable cuts of quartz for SAW applications. Epson Appl. Notes White Papers.

Lu, C.-H., Hou, T.-H., Pan, T.-M., 2018. High-performance double-gate $/alpha $ -InGaZnO ISFET pH sensor using a HfO2 gate dielectric. IEEE Trans. Electron Devices 65, 237–242. https://doi.org/10.1109/TED.2017.2776144.

Martin, N.K., Gaffney, E.A., Gatenby, R.A., Maini, P.K., 2010. Tumour-stromal interactions in acid-mediated invasion: a mathematical model. J. Theor. Biol. 267, 461–470. https://doi.org/10.1016/j.jtbi.2010.08.028.

Matsuyama, S., Llopis, J., Deveraux, Q.L., Tsien, R.Y., Reed, J.C., 2000. Changes in intramitochondrial and cytosolic pH: early events that modulate caspase activation during apoptosis. Nat. Cell Biol. 2, 318–325. https://doi.org/10.1038/35014006.

McMullan, C., Mehta, H., Gizeli, E., Lowe, C.R., 2000. Modelling of the mass sensitivity of the Love wave device in the presence of a viscous liquid. J. Phys. D. Appl. Phys. 33, 3053–3059. https://doi.org/10.1088/0022-372/33/23/307.

McHale, G., Newton, M.I., Martin, F., 2002. Theoretical mass, liquid, and polymer sensitivity of acoustic wave sensors with viscoelastic guiding layers. J. Appl. Phys. 93 (1), 675–690.

Mishra, S.K., Gupta, B.D., 2013. Surface plasmon resonance based fiber optic pH sensor utilizing Ag/ITO/Al/hydrogel layers. Analyst 138, 2640–2646. https://doi.org/10.1039/c3an00097d.

Onen, O., Ahmad, A.A., Guldiken, R., Gallant, N.D., 2012a. Surface modification on acoustic wave biosensors for enhanced specificity. Sensors 12, 12317–12328. https://doi.org/10.3390/s120912317.

Onen, O., Guldiken, R., 2014. Investigation of guided surface acoustic wave sensors by analytical modeling and perturbation analysis. Sens. Actuators A Phys. 205, 38–46. https://doi.org/10.1016/j.sna.2013.10.021.

Onen, O., Sisman, A., Gallant, N.D., Kruk, P., Guldiken, R., 2012b. A urinary Bcl-2 surface acoustic wave biosensor for early ovarian cancer detection. Sensors 12, 7423–7437. https://doi.org/10.3390/s120607423.

Onen, Onursal, 2013. Analytical Modeling, Perturbation Analysis and Experimental Characterization of Guided Surface Acoustic Wave Sensors". Graduate Theses and Dissertations. ⟨https://scholarcommons.usf.edu/etd/4555⟩.

Pang, H.F., Fu, Y.Q., Li, Z.J., Li, Y., Ma, J.Y., Placido, F., Walton, A.J., Zu, X.T., 2013. Love mode surface acoustic wave ultraviolet sensor using ZnO films deposited on 36° Y-cut LiTaO3. Sens. Actuators A Phys. 193, 87–94. https://doi.org/10.1016/j.sna.2013.01.016.

Pantazis, A.K., Gizeli, E., Konstantinidis, G., 2010. A high frequency GaN Lamb-wave sensor device. Appl. Phys. Lett. 96, 194103. https://doi.org/10.1063/1.3427484.

Pouysségur, J., Franchi, A., L'Allemain, G., Paris, S., 1985. Cytoplasmic pH, a key determinant of growth factor-induced DNA synthesis in quiescent fibroblasts. FEBS Letters 190 (1), 115–119. https://doi.org/10.1016/0014-5793(85)80439-7.

Powell, D.A., Kalantar-Zadeh, K., Wlodarski, W., 2004. Numerical calculation of SAW sensitivity: application to ZnO/LiTaO3 transducers. Sens. Actuators A Phys. 115, 456–461. https://doi.org/10.1016/j.sna.2004.05.031.

Prabhash, P.G., Haritha, V.S., Nair, S.S., Pilankatta, R., 2017. Localized surface plasmon resonance based highly sensitive room temperature pH sensor for detection and quantification of ammonia. Sens. Actuators B Chem. 240, 580–585. https://doi.org/10.1016/j.snb.2016.08.159.

Qiu, X., Tang, R., Chen, S.J., Zhang, H., Pang, W., Yu, H., 2011. PH measurements with ZnO based surface acoustic wave resonator. Electrochem. Commun. 13, 488–490. https://doi.org/10.1016/j.elecom.2011.02.028.

Salazar, P., Garcia-Garcia, F.J., Yubero, F., Gil-Rostra, J., González-Elipe, A.R., 2016. Characterization and application of a new pH sensor based on magnetron sputtered porous WO3thin films deposited at oblique angles. Electrochim. Acta 193, 24–31. https://doi.org/10.1016/j.electacta.2016.02.040.

Shamsul Arefin, M., Bulut Coskun, M., Alan, T., Neild, A., Redoute, J.-.M., Yuce, M.R., 2014. A MEMS capacitive pH sensor for high acidic and basic solutions. In: Proceedings of the IEEE SENSORS 2014, 1792–1794. https://doi.org/10.1109/ICSENS.2014.6985373.

Shibata, M., Kato, M., Iwamoto, Y., Nomura, S., Kakiuchi, T., 2013. Potentiometric determination of pH values of dilute sulfuric acid solutions with glass combination electrode equipped with ionic liquid salt bridge. J. Electroanal. Chem. 705, 81–85. https://doi.org/10.1016/j.jelechem.2013.07.024.

Singh, S., Gupta, B.D., 2012. Fabrication and characterization of a highly sensitive surface plasmon resonance based fiber optic pH sensor utilizing high index layer and smart hydrogel. Sens. Actuators B Chem. 173, 268–273. https://doi.org/10.1016/j.snb.2012.06.089.

Srivastava, J., Barber, D.L., Jacobson, M.P., 2007. Intracellular pH sensors: design principles and functional significance. Physiology 22, 30–39. https://doi.org/10.1152/physiol.00035.2006.

Stock, C., Schwab, A., 2009. Protons make tumor cells move like clockwork. Pflug. Arch. Eur. J. Physiol. 458, 981–992. https://doi.org/10.1007/s00424-009-0677-8.

Usman Ali, S.M., Alvi, N.H., Ibupoto, Z., Nur, O., Willander, M., Danielsson, B., 2011. Selective potentiometric determination of uric acid with uricase immobilized on ZnO nanowires. Sens. Actuators B Chem. 152, 241–247. https://doi.org/10.1016/j.snb.2010.12.015.

Vonau, W., Gabel, J., Jahn, H., 2005. Potentiometric all solid-state pH glass sensors. Electrochim. Acta 50, 4981–4987. https://doi.org/10.1016/j.electacta.2005.02.084.

Wang, J., Chen, D., Xu, Y., Liu, W., 2014. Label-free immunosensor based on micromachined bulk acoustic resonator for the detection of trace pesticide residues. Sens. Actuators B Chem. 190, 378–383. https://doi.org/10.1016/j.snb.2013.08.102.

Xu, Bin, Zhang, Wei-De, 2010. Modification of vertically aligned carbon nanotubes with $RuO_2$ for a solid-state pH sensor. Electrochim. Acta 55 (8), 2859–2864. https://doi.org/10.1016/j.electacta.2009.12.099.